


Ideal MHD Limited Electron Temperature in Spherical Tokamaks

S. C. Jardin¹, N. M. Ferraro¹, W. Guttenfelder¹, S. M. Kaye¹, and S. Munaretto¹

Princeton Plasma Physics Laboratory, P.O. Box 451, Princeton, New Jersey 08543 USA

 (Received 1 March 2022; revised 9 May 2022; accepted 24 May 2022; published 14 June 2022)

It is well documented that the central electron temperature in the national spherical torus experiment (NSTX) remains largely unchanged as the external heating power, and hence the normalized volume averaged plasma pressure β increases [Stutman, *Phys. Rev. Lett.* **102**, 115002 (2009)]. Here we present a hypothesis that low n , pressure driven ideal magnetohydrodynamic (MHD) instabilities that are non-disruptive, can break magnetic surfaces in the central region and thereby flatten the electron temperature profiles. We demonstrate this mechanism in a 3D resistive MHD simulation of a NSTX discharge. By varying the toroidal magnetic field strength, and/or the heating power, we show that there is a critical value of β , above which the central temperature profile no longer peaks on axis.

DOI: [10.1103/PhysRevLett.128.245001](https://doi.org/10.1103/PhysRevLett.128.245001)

Global energy confinement times for boronized wall, H -mode plasmas in the NSTX spherical tokamak (ST) were observed to have a near-linear B_T scaling, stronger than typically observed at the conventional aspect ratio [1,2]. This is also observed in other STs such as MAST [3] and Globus-M and -M2 [4,5]. Dimensionless analysis and dedicated scans illustrate that the strong B_T scaling is related largely to a strong inverse dependence of gyro-Bohm-normalized confinement times with normalized collision frequency [6,7]. For high- B_T , low- ν_* discharges, corresponding electron temperature profiles are observed to be broadened, i.e., gradients in the outer radius steepen while T_e at the magnetic axis remains largely unchanged [1,6]. In contrast, ion temperatures increase across the entire profile, largely following neoclassical predictions.

The favorable reduction of electron thermal diffusivity in the outer region of these plasmas is in part predicted due to the favorable collisionality scaling of microtearing mode transport [8,9] and possible dissipative trapped electron modes [10,11]. However, core T_e flattening and change in χ_e cannot be explained simply by ∇T_e -driven drift wave mechanisms. Multiple hypotheses have been put forth for explaining this behavior. In Ref. [12], a correlation was observed between the number and strength of high frequency global Alfvén eigenmodes and compressional Alfvén eigenmodes (CAE), which has been hypothesized to significantly enhance near-axis electron thermal transport via orbit stochasticization [13–15]. The coupling of CAE modes to kinetic Alfvén waves that can damp energy at the midradius is also predicted to modify (i.e., broaden) neutral beam injection power deposition, which can influence plasma heating in the core region [16]. However, the estimated magnitude of transport and/or energy coupling from these mechanisms is not typically large enough to entirely explain the NSTX observations [17].

Here, we address an additional hypothesis that low- n , core, ideal magnetohydrodynamic (MHD) instabilities that are nondisruptive can break up flux surfaces, ultimately leading to enhanced stochastic transport that preferentially influences electron thermal losses.

The microturbulence codes normally assume that good magnetic flux surfaces exist, which should be the case in the absence of MHD instabilities and magnetic islands. However, what if the surfaces are locally destroyed due to the onset of ideal MHD instabilities? Could this produce additional transport and possibly explain the observed electron temperature flattening and strong B_T dependence of τ_E in STs?

Recent work by Boozer [18] shows that ideal MHD instabilities can lead to magnetic surface breakup, even for an arbitrarily small resistivity. This opens up the possibility that the surfaces could be destroyed in the vicinity of large pressure gradients, and that anomalous transport could occur by way of parallel diffusion, which is much greater than diffusion across flux surfaces. To investigate this possibility, we have applied the 3D resistive MHD code M3D-C1 [19] to some reconstructed NSTX [20] equilibrium.

Consider the equilibrium from NSTX shot 124379 at time 640 ms shown in Fig. 1. This has $RB_T = 0.418$ m-T, plasma current $I_p = 990$ kA, $\beta = 6.8\%$, $\beta_N = \beta_T(\%) \times B_T(T) \times a(m)/I_p(MA) = 3.9$, and central safety factor $q(0) = 1.29$. (A scaled version of this equilibrium was used in Ref. [21], which focused on maximizing the $n = 1$ mode.) This equilibrium is unstable to many low- n (toroidal mode number) ideal MHD modes as shown in Figs. 2 and 3.

Pressure driven, radially localized, ideal MHD modes such as these, which occur in low shear regions at pressure-gradient values below the ideal MHD infinite- n ballooning limit [22], and where the growth rate is an oscillatory

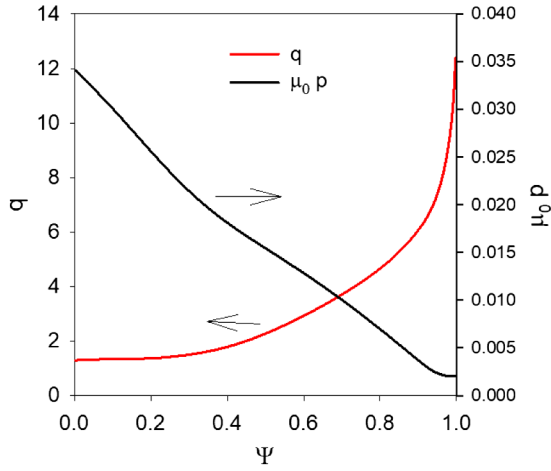


FIG. 1. Surface q profile and pressure profiles for NSTX shot 124379 at 640 ms.

function of the toroidal mode number n , have been referred to as infernal modes [23–26]. Because this equilibrium is unstable to ideal MHD modes, it is unlikely that this equilibrium file is a true representation of the experimental equilibrium at that time. Nevertheless, we evolve this configuration in time to see if it evolves into a nearby stable equilibrium state.

For simplicity, we used the single-fluid form of the 3D nonlinear M3D-C1 code to advance the particle density n , the fluid velocity \mathbf{V} , the plasma pressure p , and the magnetic scalar and vector potentials Φ and \mathbf{A} according to the following partial differential equations:

$$\frac{\partial n}{\partial t} + \nabla \cdot (n\mathbf{V}) = \nabla \cdot D\nabla n \quad (1)$$

$$\frac{\partial \mathbf{A}}{\partial t} = -\mathbf{E} - \nabla\Phi \quad (2)$$

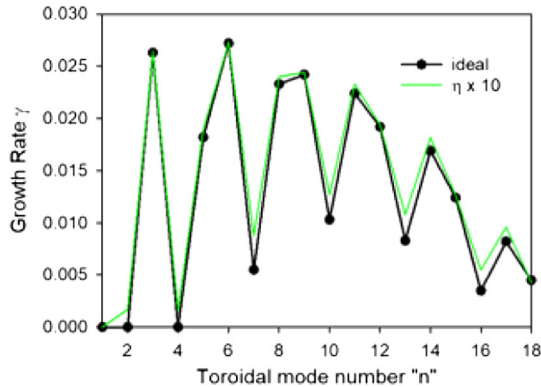


FIG. 2. Normalized growth rates for unstable modes with toroidal mode numbers 1–18 for NSTX shot 124379 640 ms. Also shown (in green online) are the growth rates with the resistivity increased by 10, indicating that these are ideal MHD instabilities.

$$\nabla_{\perp} \cdot \frac{1}{R^2} \nabla\Phi = -\nabla_{\perp} \cdot \frac{1}{R^2} \cdot \mathbf{E} \quad (3)$$

$$\mathbf{E} + \mathbf{V} \times \mathbf{B} = \eta\mathbf{J} \quad (4)$$

$$nM_i \left(\frac{\partial \mathbf{V}}{\partial t} + \mathbf{V} \cdot \nabla\mathbf{V} \right) + \nabla p = \mathbf{J} \times \mathbf{B} - \nabla \cdot \Pi \quad (5)$$

$$\frac{3}{2} \left[\frac{\partial p}{\partial t} + \nabla \cdot (p\mathbf{V}) \right] = -p\nabla \cdot \mathbf{V} + \mathbf{J} \cdot \mathbf{E} - \nabla \cdot \mathbf{q} + S_E. \quad (6)$$

The magnetic field and current density are then determined by $\mathbf{B} = \nabla \times \mathbf{A}$ and $\mathbf{J} = \nabla \times \mathbf{B}$. The symbol ∇_{\perp} in Eq. (3) refers to the gradient in the (R, Z) plane in a (R, ϕ, Z) cylindrical coordinate system. Equation (3) follows from the gauge condition on \mathbf{A} , $\nabla_{\perp} \cdot R^{-2}\mathbf{A} = 0$. The temperature is the pressure divided by the density, $T \sim p/n$. The linear form of the code used for linear stability studies is just the linearized form of these same equations.

The particle diffusion term D in Eq. (1) is a small term included to aid numerical stability. The resistivity η in Eq. (4) is the temperature-dependent Spitzer function [27] with no enhancement. The stress tensor in Eq. (5) is of standard form for viscosity [28], with viscosity coefficient μ . The heat conduction \mathbf{q} in Eq. (5) has both an isotropic part and a part parallel to the magnetic field: $\mathbf{q} = -\kappa\nabla T - \kappa_{\parallel}\nabla_{\parallel}T$.

The M3D-C1 code uses finite elements in all three dimensions. In the (R, Z) plane these are unstructured triangles that, for most of these calculations, vary in size from $h = 4$ cm near the separatrix to 1 cm near the axis. This grid, with 10346 elements per plane we call Grid A. As a convergence test, we also redid some of the calculations on a Grid B with 28792 elements per plane which vary in size from 2 cm near the separatrix to 1 cm near the axis, and on a Grid C with 38063 elements per plane varying from 1.5 cm to 1.0 cm. In the toroidal direction we used

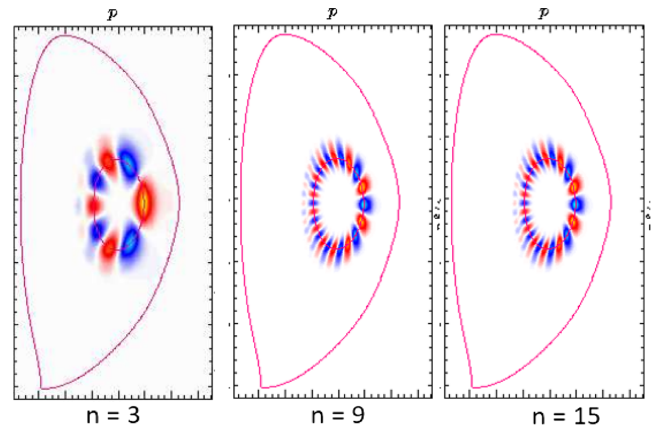


FIG. 3. Linear eigenmodes showing pressure contours for modes with $n = 3, 9$, and 15 from Fig. 2. Other modes have similar structure, with poloidal mode number $m \sim (4/3)n$.

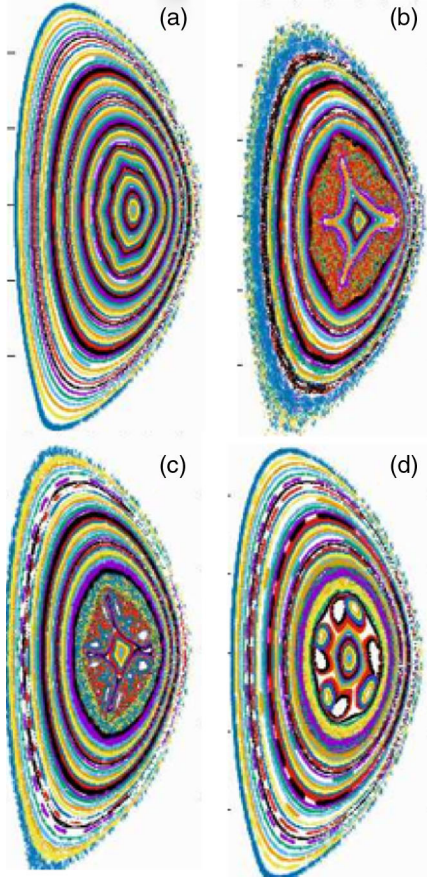


FIG. 4. Poincaré plots of the 3D M3D-C1 simulation at times (a) $t = 0$, (b) $t = 500\tau_A$, (c) $t = 600\tau_A$, and (d) $t = 6000\tau_A$.

24 planes with structured equally spaced Hermite cubic finite elements, but also performed convergence studies with 36 and 48 planes. Within each 3D toroidal prism element is a polynomial in (R, ϕ, Z) with 72 coefficients. The numerical error should vary as h^5 within a plane and h^4 in the toroidal direction.

This evolution was for 6000 Alfvén times, τ_A , corresponding to about 2.75 ms. We used very small dimensionless transport coefficients to avoid them changing the profiles significantly by themselves, and to avoid the need for a density and energy source. (Ohmic heating was present but was negligible for the resistivity and timescales involved.) The plasma current was maintained at the initial level by adjusting the loop voltage at the boundary. In code units, the dimensionless values were $D = 10^{-6}$, $\kappa = 10^{-6}$, and $\mu = 10^{-6}$. (To get the values in m^2/s , divide by $\tau_A = 4.58 \times 10^{-7}$ s.) In contrast, the dimensionless parallel thermal conductivity was $\kappa_{\parallel} = 10$, 7 orders of magnitude greater than κ . In code dimensionless units, the resistivity on axis corresponding to the Spitzer resistivity of a 916 eV plasma was initially $\eta = 2 \times 10^{-8}$.

We show Poincaré plots of the configuration at four times in the evolution in Fig. 4. The initial configuration

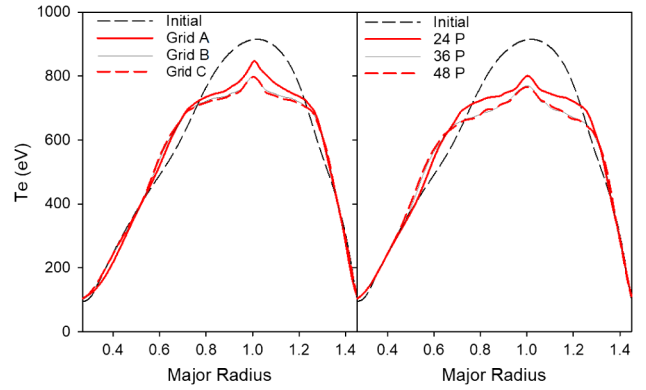


FIG. 5. Midplane temperature profiles for the initial state and for the results of the calculation at $t = 1200\tau_A$ using (left) Grid A, Grid B, and Grid C with 24 planes, and (right) Grid B with 24, 36, and 48 planes.

was linearly unstable as we saw in Figs. 2 and 3. Nonlinearly, the $n = 3$ mode grows largest and around the time $t = 500\tau_A$ deforms the surfaces, primarily those near $q = 4/3$ with a dominantly $m = 4$ poloidal variation. The stochastic region near and interior to that surface causes the temperature and pressure to drop there, restabilizing the plasma. At the final time, $t = 6000\tau_A$ in Fig. 4, the configuration is again stable with only a small dominantly $n = 3$ toroidal variation.

We show in Fig. 5 the midplane temperature profile for the initial state and the results at time $t = 1200\tau_A$ for calculations using Grid A, Grid B, and Grid C with 24 planes, and Grid B with 24, 36, and 48 planes. It is seen that the temperature has decreased significantly in the center, near the magnetic axis, but has actually increased at midradius. Thus, the result of the ideal instabilities and associated parallel transport on the ergodic field lines was to effectively increase the transport in the center, near the original magnetic axis. The fact that the results obtained on Grid B and Grid C on the left figure and with 36 and 48 planes on the right figure nearly overlay one another gives us some confidence that the results are sufficiently converged. This increase of the effective thermal conductivity in the center, over that which would be expected from microinstabilities alone, may explain similar experimental observations [12].

To further study and better quantify the effect of the ideal instabilities, we have generated a family of initial equilibrium states by applying Bateman scaling [29] to the initial equilibrium reconstruction. This scaling leaves the toroidal current density, $Rp' + R^{-1}FF'$, unchanged but increases or decreases the toroidal field strength by a factor of F_S at the separatrix. We generated two additional initial equilibrium states by setting this factor to be $F_S = 0.9$ and $F_S = 1.1$. This generated additional initial equilibrium with $[\beta = 8.2\%, q(0) = 1.2]$ and $[\beta = 5.8\%, q(0) = 1.4]$ respectively.

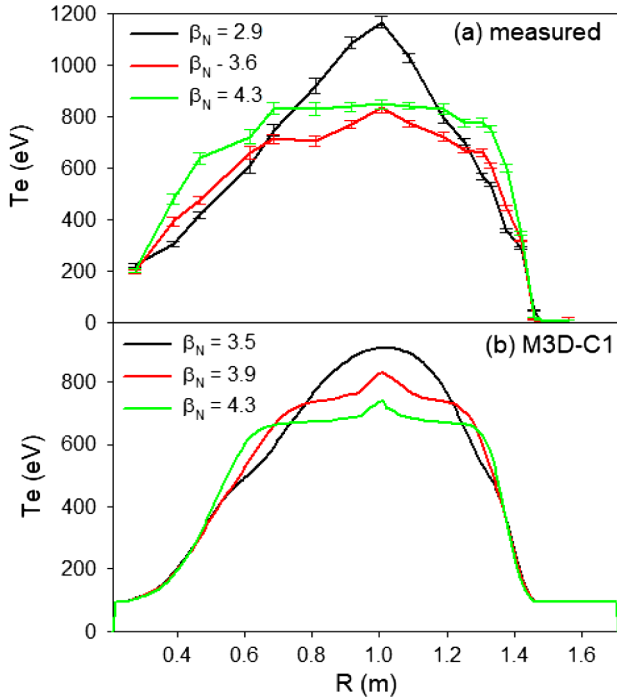


FIG. 6. (a) Experimental midplane electron temperature for the three equilibria considered in Refs. [12,30]. (b) M3D-C1 midplane electron temperature at time $t = 1200\tau_A$ starting from the three Bateman scaled equilibria corresponding to $F_S = 1.1$, $F_S = 1.0$ (the original), and $F_S = 0.9$.

We redid the calculation with each of these initial equilibrium states and plotted the midplane electron temperature at $t = 1200\tau_A$ for these and the original configuration in Fig. 6(b).

The profile labeled $\beta_N = 3.5$ in Fig. 6(b) corresponds to an equilibrium configuration with $F_S = 1.1$ that was MHD stable, and so it retained good nested magnetic surfaces, and the central temperature changed little from its initial value. The curve labeled $\beta_N = 3.9$ was taken from the equilibrium used in Fig. 5, with $F_S = 1.0$. The destruction of the magnetic surfaces in the center led to a central flattening of the temperature profile. The curve labeled $\beta_N = 4.3$ corresponds to an equilibrium with $F_S = 0.9$ that was initially even more unstable than that of the original equilibrium, and that increased instability led to a larger region in the center with destroyed surfaces and flattened temperature profile.

Each of the two unstable equilibria were linearly unstable to many modes, but the dominant nonlinear mode in the $F_S = 0.9$ case was the (5,4) (poloidal, toroidal) mode, whereas for the $F_S = 1.0$ case it was the (4,3) mode. This shift was likely due to the change in the q -profile and associated rational surfaces due to the change in the toroidal field.

In Fig. 6(a) we plot three experimentally measured midplane electron temperature profiles taken from the shots analyzed in Refs. [12,30]. While not meant to be

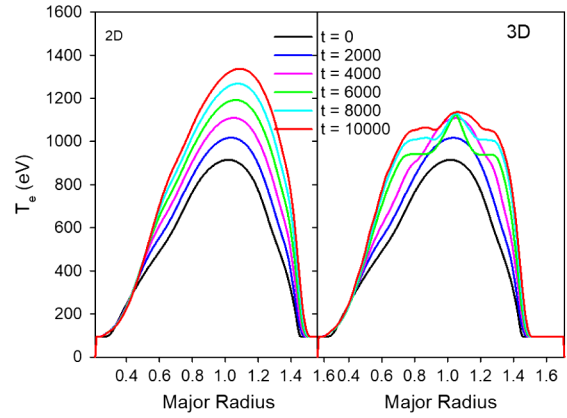


FIG. 7. Midplane electron temperature at the initial and five additional times for the 3D calculation (right) and for a 2D calculation with the same transport coefficients and heat source (left).

an exact comparison, we see the same qualitative behavior between the experimental profiles in (a) and the simulation profiles in (b). At low enough β_N the profiles are most peaked. As β_N increases, the profiles flatten near the axis, but steepen at midradius. The simulations seem to have reproduced the most dominant experimental characteristic.

This scan was somewhat unphysical because the scaled equilibrium with $F_S = 1.0$ and $F_S = 0.9$ were unstable and so unlikely to have occurred in an experiment. In an attempt to make a more physical calculation, we began with the stable equilibrium with $F_S = 1.1$, applied a heating source, and ran for $10\,000\tau_A$, or about 4.6 ms. The heating source had spatial dependence $S_E \sim \exp\{-[(R - R_0)^2 + (Z - Z_0)^2]/\delta^2\}$ where $R_0 = 1.0$, $Z_0 = 0.0$, and $\delta = 0.4$ m. To shorten the calculation we applied an unrealistically large heating source of 32 MW. The resulting temperature profiles at the initial and five additional times are shown in Fig. 7 along with those in a companion 2D calculation with the same transport coefficients and heating source.

Comparing the 2D and 3D profiles from Fig. 7, we see that the first two or three time slices are essentially identical. However, at about $t = 6000\tau_A$, corresponding to 2.75 ms when the β had increased from 5.8% to 8.4%, the primary effect of the heating was to broaden the 3D calculation temperature profile, not uniformly increase it as in the 2D calculation. This broadening of the temperature profile as β increases is qualitatively similar to the NSTX experimental result presented in Ref. [12].

In summary, we have demonstrated a new mechanism that could limit the central temperature and peakedness of the pressure profile in a ST. There are indications that this also occurs in MAST [31], although this reference emphasizes the role of the $n = 1$ mode when $q(0) \sim 1$. The details and significance of this mechanism clearly depend on the form of the pressure and current profiles and need to be further explored for a range of discharges. However, it is

clear that the possible destruction of surfaces by ideal MHD instabilities should be taken into account when performing data analysis and when projecting ST parameters for future devices.

There are reports of confinement degradation in high- β operation of conventional aspect ratio tokamaks as well when infernal modes are observed. This has likely occurred in JET [32,33], TFTR [34], JT60-U [35], DIII-D [36], and JT60-SA [37]. Future studies will help clarify what role the aspect ratio plays in this mechanism and how best to minimize its effects.

These studies use a fixed ratio of parallel to isotropic thermal conductivity of $\kappa_{\parallel}/\kappa = 10^7$ which was somewhat artificial and arbitrary. We have found that the final results depend only weakly on this ratio since for sufficiently high values, the process is self-regulating as the large parallel transport reduces the local pressure gradient and thus removes the drive, returning the configuration to a stable state.

It is also worth noting that the M3D-C1 code has a “reduced MHD” option that advances only the poloidal flux, the vorticity, and the pressure [19]. The infernal modes shown in Figs. 2 and 3 were not found with that option, and so future analysis studies should use the full MHD model as was done here.

This work was supported by the U.S. DOE Award No. DE-AC02-09CH11466, and the SciDAC Center for Tokamak Transient Simulations (CTTS). The authors acknowledge essential software support from J. Chen and the SCOREC team at RPI.

-
- [1] S. M. Kaye, R. E. Bell, D. Gates, B. P. LeBlanc, F. M. Levinton, J. E. Menard, D. Mueller, G. Rewoldt, S. A. Sabbagh, W. Wang, and H. Yuh, *Phys. Rev. Lett.* **98**, 175002 (2007).
- [2] S. M. Kaye, F. M. Levinton, D. Stutman, K. Tritz, H. Yuh, M. G. Bell, R. E. Bell, C. W. Domier, D. Gates, W. Horton *et al.*, *Nucl. Fusion* **47**, 499 (2007).
- [3] M. Valovic, R. Akers, G. Cunningham, L. Garzotti, R. Lloyd, D. Muir, A. Patel, D. Taylor, M. Turnyanskiy, and M. Walsh, *Nucl. Fusion* **49**, 075016 (2009).
- [4] G. S. Kurskiev, N. N. Bakharev, V. V. Bulanin, F. V. Chernyshev, V. K. Gusev, N. A. Khromov, E. O. Kiselev, V. B. Minaev, I. V. Miroshnikov, E. E. Mukhin *et al.*, *Nucl. Fusion* **59**, 066032 (2019).
- [5] G. S. Kurskiev, V. K. Gusev, N. V. Sakharov, I. M. Baiachenkov, E. O. Kiselev, N. A. Khromov, V. B. Minaev, I. V. Miroshnikov, M. I. Patrov, A. V. Petrov *et al.*, *Nucl. Fusion* **61**, 064001 (2021).
- [6] S. M. Kaye, S. Gerhardt, W. Guttenfelder, R. Maingi, R. E. Bell, A. Diallo, B. P. LeBlanc, and M. Podesta, *Nucl. Fusion* **53**, 063005 (2013).
- [7] S. M. Kaye, J. W. Connor, and C. M. Roach, *Plasma Phys. Controlled Fusion* **63**, 123001 (2021).
- [8] W. Guttenfelder, J. Candy, S. M. Kaye, W. M. Nevins, R. E. Bell, G. W. Hammett, B. P. LeBlanc, and H. Yuh, *Phys. Plasmas* **19**, 022506 (2012).
- [9] W. Guttenfelder, J. L. Peterson, J. Candy, S. M. Kaye, Y. Ren, R. E. Bell, G. W. Hammett, B. P. LeBlanc, D. R. Mikkelsen, W. M. Nevins, and H. Yuh, *Nucl. Fusion* **53**, 093022 (2013).
- [10] W. Wang, S. Ethier, Y. Ren, S. Kaye, J. Chen, E. Startsev, Z. Lu, and Z. Q. Li, *Phys. Plasmas* **22**, 102509 (2015).
- [11] W. Wang, S. Ethier, Y. Ren, S. Kaye, J. Chen, E. Startsev, and Z. Lu, *Nucl. Fusion* **55**, 122001 (2015).
- [12] D. Stutman, L. Delgado-Aparicio, N. Gorelenkov, M. Finkenthal, E. Fredrickson, S. Kaye, E. Mazzucato, and K. Tritz, *Phys. Rev. Lett.* **102**, 115002 (2009).
- [13] N. Gorelenkov, D. Stutman, R. Tritz, A. Boozer, L. Delgado-Aparicio, E. Fredrickson, S. Kaye, and R. White, *Nucl. Fusion* **50**, 084012 (2010).
- [14] N. Crocker, W. A. Peebles, S. Kubota, J. Zhang, R. E. Bell, E. D. Fredrickson, N. N. Gorelenkov, B. P. LeBlanc, J. E. Menard, M. Podesta *et al.*, *Plasma Phys. Controlled Fusion* **53**, 105001 (2011).
- [15] N. Crocker, E. D. Fredrickson, N. N. Gorelenkov, W. A. Peebles, S. Kubota, R. E. Bell, A. Diallo, B. P. LeBlanc, J. E. Menard, M. Podesta, K. Tritz, and H. Yuh, *Nucl. Fusion* **53**, 043017 (2013).
- [16] E. V. Belova, N. N. Gorelenkov, N. A. Crocker, J. B. Lestz, E. D. Fredrickson, S. Tang, and K. Tritz, *Phys. Plasmas* **24**, 042505 (2017).
- [17] N. A. Crocker, S. Kubota, W. A. Peebles, T. L. Rhodes, E. D. Fredrickson, E. Belova, A. Diallo, B. P. LeBlanc, and S. A. Sabbagh, *Nucl. Fusion* **58**, 016051 (2018).
- [18] A. H. Boozer, The rapid destruction of toroidal magnetic surfaces, *Phys. Plasmas* **29**, 022301 (2022).
- [19] S. C. Jardin, N. Ferraro, J. Breslau, and J. Chen, *Comput. Sci. Discovery* **5**, 014002 (2012).
- [20] M. Ono, S. M. Kaye, Y.-K. M. Peng *et al.*, *Nucl. Fusion* **40**, 557 (2000).
- [21] J. A. Breslau, M. S. Chance, J. Chen, G. Y. Fu, S. Gerhardt, N. Gorelenkov, S. C. Jardin, and J. Manickam, *Nucl. Fusion* **51**, 063027 (2011).
- [22] D. Dobrott, D. B. Nelson, J. M. Greene, A. H. Glasser, M. S. Chance, and E. A. Frieman, *Phys. Rev. Lett.* **39**, 943 (1977).
- [23] L. Zakharov, *Nucl. Fusion*, **18**, 335 (1978).
- [24] R. Dewar, J. Manickam, R. Grimm, and M. Chance, *Nucl. Fusion* **21**, 493 (1981).
- [25] J. Manickam, N. Pomphrey, and A. Todd, *Nucl. Fusion* **27**, 1461 (1987).
- [26] L. A. Charlton, B. A. Carreras, and V. E. Lynch, *Phys. Fluids B* **2**, 1574 (1990).
- [27] J. D. Huba, NRL Plasma Formulary, Naval Research Laboratory NRL/PU/6790—13-589, Revised (2013).
- [28] L. D. Landau and E. M. Lifschitz, *Fluid Mechanics*, 1st ed. (Pergamon Press, New York, 1959), Vol. 6.
- [29] G. Bateman and Y.-K. M. Peng, *Phys. Rev. Lett.* **38**, 829 (1977).
- [30] $\beta_N = 2.9$: NSTX shot 120451@400 ms, $\beta_N = 3.6$: NSTX shot 120434@400 ms, $\beta_N = 4.3$: NSTX shot 120446@400 ms.

- [31] I. T. Chapman, W. A. Cooper, J. P. Graves, M. P. Gryaznevich, R. J. Hastie, T. C. Hender, D. F. Howell, M. D. Hua, G. T. Huysmans, D. I. Keeling *et al.*, *Nucl. Fusion* **51**, 073040 (2011).
- [32] O. J. Kwon, I. T. Chapman, P. Buratti, H. Han, Y. Na *et al.*, *Plasma Phys. Controlled Fusion* **54**, 045010 (2012).
- [33] L. A. Charlton, L. R. Baylor, A. W. Edwards, G. W. Hammett, W. A. Houlberg, P. Kupschus, V. E. Lynch, S. L. Milora, J. O'Rourke, and G. L. Schmidt, *Nucl. Fusion* **31**, 1835 (1991).
- [34] Z. Chang, E. D. Fredrickson, J. D. Callen, K. M. McGuire, M. G. Bell, R. V. Budny, C. E. Bush, D. S. Darrow, A. C. Janos, L. C. Johnson *et al.*, *Nucl. Fusion* **34**, 1309 (1994).
- [35] T. Ozeki, M. Azumi, Y. Kamada, S. Ishida, Y. a. Neyatani, and S. Tokuda, *Nucl. Fusion* **35**, 861 (1995).
- [36] A. D. Turnbull, D. P. Brennan, M. S. Chu, L. L. Lao, and P. B. Snyder, *Fusion Sci. Technol.* **48**, 875 (2005).
- [37] A. Bierwage, M. Toma, and K. Shinohara, *Plasma Phys. Controlled Fusion* **59**, 125008 (2017).